



# Co supported on N and S dual-doped reduced graphene oxide as highly active oxygen-reduction catalyst for direct ethanol fuel cells

S. Fajardo<sup>a</sup>, P. Ocón<sup>b,\*</sup>, J.L. Rodríguez<sup>a</sup>, E. Pastor<sup>a,\*</sup>

<sup>a</sup> Instituto de Materiales y Nanotecnología, Departamento de Química, Universidad de La Laguna, PO Box 456, 38200 La Laguna, Santa Cruz de Tenerife, Spain

<sup>b</sup> Universidad Autónoma de Madrid, Departamento de Química Física Aplicada, C/Francisco Tomás y Valiente 7, 28049 Madrid, Spain

## ARTICLE INFO

### Keywords:

Direct ethanol fuel cell  
Oxygen reduction reaction  
Reduced graphene oxide  
Heteroatom-doped graphene materials, non-noble metal catalyst

## ABSTRACT

Oxygen reduction reaction (ORR) is one of the key features for the efficient functioning of several energy conversion devices such as fuel cells, appearing the necessity of development of new low-cost catalyst materials. Heteroatom-doped carbon materials have attracted attention in this field due to its physicochemical and electronic properties. In this work, a nitrogen and sulfur doped material with anchored  $\text{Co}_3\text{O}_4$  nanoparticles (Co/SN-rGO) is proposed as cathode catalyst for direct ethanol fuel cells (DEFCs) and results are compared with different doped graphene nanomaterials (GMs). The effect of the heteroatoms and cobalt oxide nanoparticles in the final efficiency was studied. Synthesized materials were characterized and the activity of Co/SN-rGO and GMs for the ORR was studied. Co/SN-rGO presents high ORR performance in terms of onset potential ( $E_{\text{onset}}$ ), 0.86 V (vs RHE) and half-wave potential ( $E_{1/2}$ ) 0.72 V (vs RHE). Tafel analysis shows 60 mV dec<sup>-1</sup> at low overpotential for potential dependent ORR mechanism. Besides, when Co/SN-rGO performance is evaluated in a DEFC using a fuel cell test station, main results indicate higher catalytic activity, stability, and ethanol tolerance of Co/SN-rGO in comparison to a carbon-supported Pt catalyst.

## 1. Introduction

Polymer exchange membrane fuel cells (PEMFCs) are promising green energy generation technology since they can convert chemical energy stored in fuels directly into electrical energy through electrochemical reactions with high power density [1]. Hydrogen is one of the most used fuels for these devices. However, low molecular weight organic molecules such as methanol, ethanol or glycerol are also employed in FCs because of their higher energy density and their facilities in transporting and storing comparing to hydrogen, which makes direct alcohol fuel cells (DAFCs) suitable for portable devices [2,3]. Furthermore, it is remarkable in the case of ethanol that it can be obtained from biomass, which is very interesting from an environmental point of view [2,4].

High energy conversion efficiency is needed in these electrochemical systems, which conditions the use of catalyst for both, cathodic and anodic reactions. Thus, finding an efficient oxygen reduction reaction catalyst is challenging due to the sluggish kinetics of this reaction [5]. Moreover, it has been demonstrated that anode and cathode kinetics are substantially improved when the device operates in alkaline medium [1,6]. Platinum based materials are those that offer better performance

in spite of its drawbacks such as their susceptibility to CO poisoning and high cost, which rise the manufacturing costs, making the development of Pt-free catalysts an important topic in FC research [7].

Most promising results in this field are obtained using heteroatom doped carbon based materials supporting metals, specially metal-nitrogen-carbon catalysts (M–N–C) [8]. Co is proposed as one of the main nonprecious catalyst for the ORR because of its high durability in alkaline medium, natural abundance and low price [9]. More concretely cobalt oxide based catalysts have demonstrated great electrocatalytic properties for the ORR [10]. Although  $\text{Co}_3\text{O}_4$  allows the improvement of ORR kinetics, their low electrical conductivity and surface area makes it difficult to obtain an adequate performance. Beside this,  $\text{Co}_3\text{O}_4$  catalytic properties decrease because aggregation occurs during their use [11]. In order to alleviate these deficiencies, some strategies are developed; thus, the combination of  $\text{Co}_3\text{O}_4$  with carbonaceous materials with large surface area and conductivity can be found in the bibliography [11–14].

Graphene based materials have demonstrated good electrocatalytic activity towards the ORR [15–17] and extraordinary tolerance to alcohol oxidation [18,19]. The introduction of heteroatoms such as N, B, S, P or F into the graphene structure, with electron-acceptor or electron-donor properties, induces asymmetry spin density, and finally,

\* Corresponding authors.

E-mail addresses: [pilar.ocon@uam.es](mailto:pilar.ocon@uam.es) (P. Ocón), [epastor@ull.edu.es](mailto:epastor@ull.edu.es) (E. Pastor).

<https://doi.org/10.1016/j.cej.2023.142053>

Received 13 October 2022; Received in revised form 9 February 2023; Accepted 19 February 2023

Available online 22 February 2023

1385-8947/© 2023 The Authors. Published by Elsevier B.V. This is an open access article under the CC BY license (<http://creativecommons.org/licenses/by/4.0/>).

modulates the electronic properties of the material, enhancing its electrocatalytic behavior [20]. Although it is not fully understood the mechanism by which nitrogen facilitates the ORR, it is well known that its activity largely depends on the type of nitrogen, being the pyridinic group the one that offers the best results [21,22]. Zhang *et al.* found that the introduction of nitrogen atoms produces a modification of the atomic charge and spin distribution of graphene sheets that makes the neighboring carbon atoms more favorable for oxygen adsorption and facilitates the further steps in the reaction path [23,24]. The presence of sulfur atoms in graphene structures allows an improvement in the conductivity of the material thanks to its electron donor character and its low effect on the charge mobility of grapheme [25–27]. Several investigations have reported that the simultaneous introduction of nitrogen and sulfur functionalities in carbonaceous materials can enhance its electrocatalytic properties [7,28]. In addition, the incorporation of electron-rich atoms in the graphene structure and the presence of oxygenated functionalities such as ketones, aldehydes, carboxylic acids, or quinone and hydroquinone groups, among others, can produce crystalline defects that favor the anchoring of nanoparticles and modify the properties of the materials, i.e. basicity/acidity or hydrophilicity/hydrophobicity, which can help to prevent the cathode flooding in the fuel cell performance [29].

In this work, reduced graphene oxide doped with sulphur and nitrogen is proposed as a support material for Co<sub>3</sub>O<sub>4</sub> nanoparticles (Co/SN-rGO). The electrocatalytic activity of this catalyst towards the ORR is studied and compared to other doped reduced graphene oxide (rGO) catalyst. Furthermore, Co/SN-rGO performance was evaluated as cathode catalyst in a direct ethanol fuel cell and compared with a commercial carbon-supported Pt catalyst. For this purpose, X-rGO (X = S, N, and SN) were synthesized and physicochemical and electrochemical characterizations have been carried out. This study provides a deeper insight on the effect of the presence of N and S on the ORR. Main results indicate higher catalytic activity, stability, and ethanol tolerance of Co/SN-rGO compared to Pt material.

## 2. Experimental

### 2.1. Graphene oxide synthesis

Graphene oxide was synthesized by modification of the Hummers method [7]. Briefly, 3.5 g of KMnO<sub>4</sub> (>99.8 %, Panreac) were slowly added into a 250 mL Erlenmeyer flask containing 30 mL of H<sub>2</sub>SO<sub>4</sub> (Merck p.a.) and 1 g of graphite (Sigma-Aldrich). Then, the mixture was diluted to 80 mL using ultrapure water (18.2 M Ω cm) and stirred for 1 h at 35 °C. After that, the solution was heated up to 95 °C for 15 min and diluted to 200 mL with ultrapure water. Next, 1.25 mL of H<sub>2</sub>O<sub>2</sub> (30 % v/v, Foret) was slowly added. The solution was stirred for 24 h, and then, centrifuged with ultrapure water until a pH of about 7 was achieved in the supernatant. Finally, the GO was dried at 60 °C in an oven.

### 2.2. Reduced graphene oxide (rGO) synthesis

GO reduction was carried out by thermal treatment under a reductive atmosphere (5 % H<sub>2</sub>/95 % N<sub>2</sub> at 100 mL/min) in a tubular furnace. Basically, the GO was treated with a temperature ramp of 5 °C/min from room temperature up to 200 °C. Once the temperature was reached, it was maintained for 30 min, after which, a new temperature ramp of 5 °C/min started and heated up to 450 °C, where it was maintained for 1 h. Then, it was cooled to room temperature obtaining a black powder.

### 2.3. Doped reduced graphene oxide synthesis

Doped reduced graphene materials were obtained by hydrothermal reduction of GO. Briefly, 0.15 g of GO were dispersed in 30 mL ultrapure water, after that 4 mmol of reducing agent were added to the aqueous dispersion, introduced in a 45 mL Teflon reactor, and heated at 160 °C

for 10 h. The resulting aqueous dispersion was repeatedly centrifuged with ultrapure water and then dried in an oven at 60 °C for 24 h. The reducing agents were sodium bisulfite (>99 %, Sigma-Aldrich) and thiourea (>99 %, Fluka), obtaining S-rGO and SN-rGO, respectively.

### 2.4. Cobalt oxide deposited on SN-rGO

Cobalt oxide nanoparticles supported on SN-rGO (Co/SN-rGO) were prepared by chemical reduction of CoCl<sub>2</sub> (>98 %, Sigma-Aldrich) at room temperature using NaBH<sub>4</sub> (>99 %, Fluka) as reducing agent. For this, 16 mg of SN-rGO were dispersed in 16 mL of ultrapure water using ultrasonication during 30 min at room temperature. Then, 8.8 mg of CoCl<sub>2</sub> were slowly added and the mixture was sonicated for 10 min. Afterwards, 5 mL of 0.1 M sodium borohydride (99 %, Fluka) solution was added while the dispersion is being stirred. A black precipitate was formed, which was washed with ultrapure water using a centrifuge and dried at 60 °C in an oven. The obtained metal load was determined to be 18 wt% by energy dispersive X-Ray spectroscopy (EDX).

### 2.5. Physicochemical characterization

X-ray diffraction analysis were performed using a PANalytical X'PERT-Pro diffractometer for powder samples, applying Cu-Kα radiation ( $\lambda = 0.15406$  nm) at 40 kV and 20 mA. 2θ values scans were recorded between 5° and 100° at 0.04° s<sup>-1</sup>. The lattice parameters were obtained by refining the unit cell dimensions by the least square method. Interplanar distance and crystallite size were determined by the standard procedure published by Iwashita *et al.* [30] using Bragg's law (1) and Debye-Scherrer equation (2), respectively:

$$2d_{hkl}\sin\theta = n\lambda \quad (1)$$

$$L_c = \frac{0.9\lambda}{\beta_{1/2}\cos\theta} \quad (2)$$

where  $d_{hkl}$  is the interplanar distance,  $\theta$  is the scattering angle,  $\lambda$  is the wavelength of the incident wave,  $L_c$  is the crystallite size, and  $\beta_{1/2}$  is the full width at half maximum.

X-ray photoelectron spectroscopy (XPS) spectra were acquired using a VG Escalab200R spectrometer equipped with a hemispherical analyzer, five channeltron detectors and fitted with an MgKα ( $\lambda = 1253.6$  eV) 120 W X-ray source. XPS data were recorded under pressures below 3·10<sup>-8</sup> mbar. Binding energies (±0.2 eV) were determined by referencing to the C1s peak at 284.8 eV.

Raman spectra were recorded on a Renishaw confocal Raman Microscope spectrometer inVia model with an excitation wavelength of 532 nm. The Raman scattered light was recorded from 100 to 3200 cm<sup>-1</sup>.

Elemental analysis measurements were performed using an Elemental Analyzer CNHS FLASH EA 1112 (Thermo Scientific).

Finally, energy dispersive X-ray analyzer (Oxford 6699 ATW, Oxford, Oxfordshire, UK) was used to determine the metal load.

### 2.6. Electrochemical characterization

Electrochemical measurements were performed using an Autolab PGSTAT30 potentiostat–galvanostat (Metrohm Autolab). All the experiments were carried out in a 0.1 M NaOH (99.99 %, Sigma Aldrich) alkaline solution using a three-electrode glass cell at room temperature. A glassy carbon cylinder was used as counter electrode and a reversible hydrogen electrode (RHE) in the supported electrolyte as reference electrode. A rotating ring-disk electrode (RRDE, PINE) with a glassy carbon disk (disk diameter 5 mm) and a Pt ring (collection efficiency determined to be  $N = 0.22$ ) was utilized as working electrode. The catalyst ink was prepared by mixing 2 mg of the catalyst with 15 μL of Nafion® perfluorinated solution (5 wt% in a mixture of lower aliphatic

alcohols and water) and 500  $\mu\text{L}$  of milli-Q water. Then, 20  $\mu\text{L}$  of the ink were deposited on the glassy carbon disk of the RRDE using a micropipette and dried under nitrogen atmosphere, giving a catalyst load of 0.4  $\text{mg}\cdot\text{cm}^{-2}$ .

Before starting tests, the electrolyte was deoxygenated by bubbling Ar (99.999 %, Alpha GAZ, Air Liquide) during 15 min. An activation process, consisting of performing cyclic voltammetry (CV) in the potential range of 0.05–1.00 V, at 0.20  $\text{V}\cdot\text{s}^{-1}$  until a reproducible voltammogram is reached, and it was performed before the measurements. Then, the blank cyclic voltammogram was recorded at 0.01  $\text{V}\cdot\text{s}^{-1}$ . Afterwards, the solution was saturated with  $\text{O}_2$  (99.999 %, Alpha GAZ, Air Liquide) by bubbling it during 15 min and a cyclic voltammogram was obtained in the same conditions. For the ORR study, steady state polarization curves were acquired at 400, 600, 900, 1600 and 2500 rpm in a  $\text{O}_2$  saturated solution. For this, a linear sweep voltammetry (LSV) was performed from 1 to 0.05 V at 0.002  $\text{V}\cdot\text{s}^{-1}$ . The Pt ring potential was maintained at 1.2 V during the scans for obtaining the currents generated by the oxidation of the produced  $\text{HO}_2^-$  into  $\text{O}_2$ . Both ring and disk currents ( $I_r$  and  $I_d$ ) were recorded as a function of the disk electrode potential.

The average number of transferred electrons during the ORR, as well as the percentage of  $\text{HO}_2^-$  produced, were determined by the following equations (eq. (3) and eq. (4), respectively):

$$n = \frac{4I_d}{I_d + I_r/N} \quad (3)$$

$$\% \text{HO}_2^- = \frac{200I_r/N}{I_d + I_r/N} \quad (4)$$

where  $I_d$  is the current generated at the disk,  $I_r$  is the ring current generated at the ring, and  $N$  is the current collection efficiency of the Pt ring.

## 2.7. DEFC tests

The performance of the catalysts at the cathode of a DEFC was evaluated in a 4  $\text{cm}^2$  single cell. Tests were made by using an Arbin instrument Fuel Cell Test Station (FCTS) that operates with the MITS Pro software. Commercial Polybenzimidazole (PBI) membranes (50  $\mu\text{m}$  thickness) from Danish Power Systems were employed as polymer electrolyte. The membrane was immersed in KOH 6 M for 5 days to dope it with  $\text{OH}^-$  functionalities.

The electrodes were prepared by spraying the catalyst ink over a carbon cloth diffusion layer (ELAT GDL-LT 1200 W). The prepared inks contained the catalyst, Nafion®, isopropanol (>99.8%; Sigma-Aldrich) and Milli-Q water. A commercial 45 wt% PtRu/C catalyst (HiSPEC™ 7000, Pt-Ru 45 wt% on carbon black, Pt:Ru atomic ratio 2:1, Johnson Matthey) was used as anode catalyst. Commercial 40 wt% Pt/C (HiSPEC™ 4000, 40 wt% Pt on carbon black, Johnson Matthey) as well as the prepared Co/SN-rGO catalyst material were used as cathode. Each catalyst ink was dispersed in deionized water/isopropanol (2:1 vol) and Nafion® and finally sonicated. The total amount of Pt load at Pt-Ru and Pt-based electrodes were 1  $\text{mg}\cdot\text{cm}^{-2}$  and 1.26  $\text{mg}\cdot\text{cm}^{-2}$ , respectively, with a 4 wt% of Nafion® (dry basis). The Co/SN-rGO catalyst load was 1.26  $\text{mg}\cdot\text{cm}^{-2}$  with a Nafion® content of 7 wt%.

The membrane electrode assembly (MEA) was hot pressed at 100 °C at 60 bars for 3 min. The cell operated at 90 °C and the anode was fed with 2 M ethanol (>99.8 %; Sigma-Aldrich) and 2 M KOH solutions preheated at 80 °C at a flow rate of 1  $\text{mL min}^{-1}$ . The cathode was fed with oxygen at a flow rate of 0.2  $\text{L min}^{-1}$  without humidification with a back pressure of 3 bar. The polarization curves were recorded at 0.010  $\text{V}\cdot\text{s}^{-1}$  from open circuit potential to 0 V.

## 3. Results and discussion

Different heteroatom doped graphene materials were obtained by reducing graphene oxide with diverse reducing agents. Besides,  $\text{Co}_3\text{O}_4$  was supported on S and N dual doped reduced graphene oxide (SN-rGO) by in situ reduction of  $\text{CoCl}_2$  using  $\text{NaBH}_4$  as reducing agent.

### 3.1. Physicochemical characterization

Table 1 summarizes the content of H, N, S and O for all the studied GMs determined by elemental analysis. As shown in Table 1, SN-rGO is the catalyst with the lowest oxygen content followed by the Co/SN-rGO. The thermal reduced graphene oxide (rGO) presents 0.8 % of sulfur in its composition presumably due to  $\text{H}_2\text{SO}_4$  impurities coming from the graphene oxide synthesis by the Hummers modified method. Attending to the amount of oxygen in each material, the efficiency of the reducing procedures decreases as follows: thiourea > thermal treatment > sodium bisulfite.

XRD was performed to investigate the crystallinity of the different graphene materials. All GMs (Fig. 1a) exhibit a signal at a diffraction angle of  $26.7^\circ$  which corresponds to the (002) plane of the graphite structures [31–33]. On the other hand, chemically reduced graphene materials reveal a small peak at  $43^\circ$  associated to the (100) diffraction plane of graphitic carbon [16]. It should be noted that S-rGO shows also a third diffraction peak at  $10.7^\circ$  which can be related with the (001) diffraction plane produced by the presence of GO domains due to the partial reduction that occurs when sodium bisulfite is used as reducing agent, which agrees with the results given by elemental analysis. The slight shift of the (002) plane to lower  $2\theta$  values in GMs compared to that of graphite [7] indicates the increase of the interplanar distance (Table 2). The thickening of the (002) signal reveals the exfoliated nature of the reduced materials. In addition, a contribution at low  $2\theta$  values can be distinguished in the Co/SN-rGO diffractogram, which can be explained by the presence of crystalline cobalt oxide species.

Different crystallographic parameters are summarized in Table 2. All the catalysts show slightly higher interplanar distance compared to that of graphite (0.34 nm) because of the presence of intercalated oxygen functional groups between layers [24]. From  $d_{hkl}$  and  $L_c$  it is possible to estimate the number of graphene layers that compose each material. The number of layers drastically decreases after oxidation of graphite due to the increase in the interplanar distance which facilitates the exfoliation.

Raman spectroscopy is one of the most used techniques for the characterization of carbonaceous materials due to the information it provides on the morphological and structural changes that the material undergoes in response to the different chemical treatments to which they are subjected [27,34,35]. Fig. 1b reveals that all spectra exhibit three main bands related to graphite-like structure, known as D, G and 2D bands located at around 1350, 1580 and 2700  $\text{cm}^{-1}$ , respectively. D band is associated to  $\text{sp}^3$  carbon domains and crystallite defects while G band is related to ordered  $\text{sp}^2$  carbon domains [26]. On the other hand, 2D band ( $\sim 2710 \text{ cm}^{-1}$ ) is attributed to an overtone of the D band, which is produced by a second order resonance process and its intensity depends on the laser intensity and the number of layers [36]. Graphite ordered structure and its shape is very sensitive to the number of graphene layers [26,27]. Furthermore, GMs Raman spectra shows a fourth small feature at 2940  $\text{cm}^{-1}$  which is an overtone produced by the

**Table 1**  
Elemental composition obtained by elemental analysis.

Elemental composition (wt. %)				
Material	C	O	N	S
rGO	78.1	21.9	–	0.8
S-rGO	70.1	24.0	–	5.9
SN-rGO	75.8	13.9	2.3	8.1
Co/SN-rGO	74.1	15.8	2.2	7.9

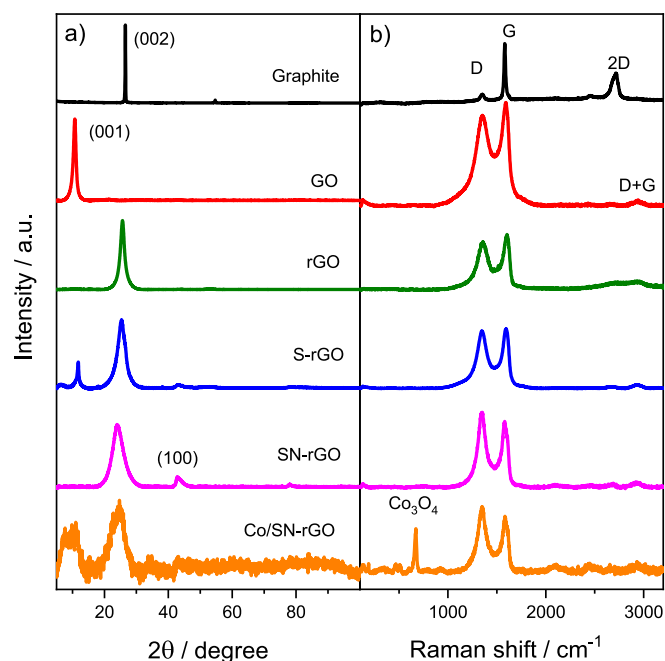


Fig. 1. A) xrd patterns and b) raman spectra for all the studied materials.

Table 2

Crystallographic parameters obtained from XRD and Raman analysis.

Material	2θ (002) / degree	Interplanar distance (d)/nm	Crystallite size (L <sub>c</sub> )/nm	Number of layers	I <sub>D</sub> /I <sub>G</sub>
Graphite	26.6	0.34	47.2	140	0.15
GO	10.7	0.84	8.2	11	0.87
rGO	25.6	0.35	2.3	8	0.86
S-rGO	25.3	0.37	1.9	6	0.96
SN-rGO	24.0	0.37	1.8	6	1.15
Co/SN-rGO	24.7	0.36	1.7	6	1.17

contribution of D and G band (denoted as D + G) [26,36]. Co/SN-rGO Raman spectrum shows three new bands located at 465, 506 and 671 cm<sup>-1</sup> that belongs to Co<sub>3</sub>O<sub>4</sub> species [17,35,37].

It is common to calculate the ratio of intensities between the D and G bands (I<sub>D</sub>/I<sub>G</sub>) to be used for the evaluation of the structural changes and the disorder degree of a given carbon material. The higher I<sub>D</sub>/I<sub>G</sub> values, the higher the disorder degree [33,38]. As seen in Table 2, rGO is the most ordered material (I<sub>D</sub>/I<sub>G</sub> = 0.86). The disorder degree increases in S-rGO catalyst due to the formation of S-C bonds. Dual doped catalysts (SN-rGO and Co/SN-rGO) have the largest I<sub>D</sub>/I<sub>G</sub> value (1.15 and 1.17, respectively) which reflects the predominance of sp<sup>3</sup> carbon atoms, possibly due to the simultaneous formation of S-C and N-C bonds [29,34,39]. The higher peak intensity of the D band with respect to that of the G band, seen in the SN-rGO and Co/SN-rGO Raman spectra given in Fig. 1b, indicates the presence of a large number of edges/defects which can provide active sites for the ORR [21,40,41].

X-ray photoelectron spectroscopy spectra are given in the supporting information (Figures S1-S5) and results are summarized in Table 3. rGO shows two sharp peaks at 532.9 and 285.9 eV related to O1s and C1s orbitals, respectively, which suggest the only presence of oxygen and carbon (Figures S1 and S2). Sulfur doped materials display a peak approx. at 165.0 eV which correspond to the S2p orbital (Figure S3), whereas the peak around 400.3 eV observed for SN-rGO and Co/SN-rGO is related to the N1s. Three contributions are apparent in the deconvoluted N1s orbital for SN-rGO (Figure S4), located at 398.9, 400.2 and 401.8 eV, which are associated with pyridinic, pyrrolic and quaternary nitrogen, respectively.

Table 3

X-Ray photoelectron spectroscopy analysis of the catalysts, binding energy of the species and percentage of each one in brackets.

Element	C1s	N1s	S2p	O1s	Co2p
<b>Catalyst</b>					
<b>rGO</b>	284.8 (56) C-C	–	–	531.3 (18) O = C 532.5 (35) OH-C 533.8 (47) O-C = O	–
<b>S-rGO</b>	284.8 (51) C-S and C-C 286.3 (32) C-O-C 287.8 (17) O-C = H	–	164.0 (85) -C-S-C- 167.8 (15) -SO <sub>x</sub> -	531.3 (27) O = C 532.5 (36) OH-C 533.8 (37) O-C = O	–
<b>SN-rGO</b>	284.8 (65) C-S and C-C 286.3 (24) C-N and C-O-C 287.7 (11) O-C = H	398.9 (33) pyridinic 400.2 (48) pyrrolic 401.8 (19) quaternary	164.0 (85) -C-S-C- 168.0 (15) -SO <sub>x</sub> -	531.3 (28) O = C 532.5 (39) OH-C 533.8 (33) O-C = O	–
<b>Co/SN-rGO</b>	284.8 (67) C-S and C-C 286.4 (25) C-N and C-O-C 287.9 (8) O-C = H	398.4 (35) pyridinic 400.2 (46) pyrrolic 401.8 (19) quaternary	163.9 (31) -C-S-C- 167.7 (69) -SO <sub>x</sub> -	531.3 (35) O = C 532.5 (42) OH-C 533.8 (23) O-C = O	779.1, 796.1 (60.91) Co <sup>3+</sup> 782.0, 797.9 (20.10) Co <sup>2+</sup> 780.1 (18.99) Co-N

Deconvolution of the S2p orbital in the spectrum for S-rGO and SN-rGO, shows two peaks that can be attributed to -C-S-C- (163.9 eV) and -SO<sub>x</sub>- (167.7 eV) [34,42] species. However, deconvolution of the S2p contribution in the spectrum of Co/SN-rGO indicates a variation of the intensities of the peaks corresponding to -C-S-C- and -SO<sub>x</sub>- type species, with the predominance of sulfoxide bonds. The later may be produced by the formation of new -SO<sub>x</sub>- groups between the sulfur atoms and the cobalt oxide species.

Finally, Co2p spectrum reveals the presence of Co<sub>3</sub>O<sub>4</sub> with two peaks at around 796.3 and 780.7 eV (Figure S5), which correspond to Co 2p<sub>1/2</sub> and 2p<sub>3/2</sub> transitions respectively. The separation between these two peaks is 15.6 eV which agrees with the literature [43]. In addition, two satellite peaks attributed to Co 2p<sub>1/2</sub> and Co 2p<sub>3/2</sub> transitions are observed at about 802 and 786 eV, respectively [39,44]. Additionally, Co 2p<sub>1/2</sub> and 2p<sub>3/2</sub> can be deconvoluted in three peaks associated to Co<sup>2+</sup> (782.0 and 797.9 eV), Co<sup>3+</sup> (779.1 and 796.1 eV) and Co-N (780.6 eV) which confirms the Co-N interactions [45].

### 3.2. Electrochemical characterization

Voltametric profiles of the catalysts in argon saturated medium



present the typical double layer response of the carbonaceous materials (Fig. 2, red lines)[29]. It is shown that rGO has the lowest capacitive currents, which can be related with the low disorder degree compared to the other catalysts. Non-faradaic processes increase after introducing heteroatoms on its structure developing higher double layer currents, especially when doping with sulfur.

On the other hand, when the CVs are performed in an oxygen saturated solution (Fig. 2, black lines), a clear reduction peak is observed for all materials except for the S-rGO, where this feature can be partially overlapped with the large capacitive currents, suggesting a more disabled ORR for this catalyst. SN-rGO and Co/SN-rGO develop the best response towards the ORR, since their cathodic peaks ( $E_{\text{peak}}$ ) are the ones located at more positive potentials, 0.75 and 0.77 V respectively (Fig. 2).

In addition, RRDE linear sweep voltammetry measurements were carried out for further evaluation of the ORR performance of the as-prepared catalysts. Co/SN-rGO is the material that presents the lowest overpotential for the ORR (Fig. 3a), with an onset potential of 0.86 V, shifted around 90 mV to more positive potentials compared to those of SN-rGO and S-rGO, and 140 mV compared to rGO. Moreover, Co/SN-rGO develops the highest cathodic current densities. S-rGO shows the same limit current density ( $j_L$ ) and similar onset potential to that of SN-rGO (0.81 V) (Table 4); however, the lower slope in the mixed control region of the polarization curve suggests a more hindered oxygen reduction for the S-rGO. The percentage of  $\text{HO}_2^-$  intermediate produced during the ORR determined using eq. (4) (inset in Fig. 3c), confirms that the amount of these species decreases as follows: rGO > S-rGO > SN-rGO > Co/SN-rGO. This is in accordance with the potential at  $-1 \text{ mA/cm}^2$ , which increase inversely to the production of  $\text{HO}_2^-$ : Co/SN-rGO > SN-rGO > S-rGO > rGO.

The ORR can occur through two routes known as 2- and 4-electrons pathways. In the 4-electrons pathway, oxygen is reduced directly to hydroxide (eq. (5)), while in the 2-electrons route (eqs. (6) and (7)), a hydroperoxide intermediate is generated, which is known that can degrade the polymer electrolyte in this type of fuel cells [46].



Consequently, it is important to establish the mechanism of the ORR at these materials. The number of electrons ( $n$ ) transferred during the ORR were determined as a function of the potential from LSV data using eq. (3) (Fig. 3b). Co/SN-rGO shows a four electrons pathway for  $E < 0.80 \text{ V}$  ( $n \sim 3.9$ ). The value of  $n$  for SN-rGO is about 3.85 electrons at 0.7 V and slowly decreases achieving approx. 3.7 at 0.1 V. On the other

hand, rGO is the material with the lowest  $n$  value ( $\sim 3.4$ ). It is concluded that the ORR occurs at Co/SN-rGO and SN-rGO mainly by the 4-electrons pathway, while for the other catalysts four and two electrons routes occur simultaneously. This is in accordance with the %  $\text{HO}_2^-$  calculated, which decreases in the following order: rGO > S-rGO > N-rGO (previous work [71]) > SN-rGO > Co/SN-rGO (inset in Fig. 3b). These results confirm the ability of doping to improve the electrocatalytic activity of graphene materials. Moreover, the synergistic effect of S and N co-doping against the ORR and the capacity of  $\text{Co}_3\text{O}_4$  for heterogeneous decomposition of  $\text{H}_2\text{O}_2$  in alkaline medium are verified.

For a mixed transport-kinetic controlled process, the reciprocal of the measured current density can be expressed as a sum of the reciprocals of the kinetic and limiting current densities (Koutecky-Levich equation (K-L)):

$$\frac{1}{j} = \frac{1}{j_k} + \frac{1}{j_L} = \frac{1}{j_k} + \frac{1}{0.62nFD_{\text{O}_2}^{2/3} \nu^{-1/6} C_{\text{O}_2} \omega^{1/2}} \quad (8)$$

where  $j$  is the measured current density,  $j_k$  and  $j_L$  are the kinetic and the diffusion-limited current densities, respectively,  $n$  is the number of electrons transferred during the process,  $F$  is the Faraday constant (96485C/mol),  $C_{\text{O}_2}$  is the saturation concentration of oxygen ( $1.13 \cdot 10^{-6} \text{ mol cm}^{-3}$ ),  $D_{\text{O}_2}$  is the diffusion coefficient of oxygen ( $2.22 \cdot 10^{-5} \text{ cm}^2 \text{ s}^{-1}$ ),  $\nu$  is the kinematic viscosity of the solution ( $1.1 \cdot 10^{-2} \text{ cm}^2 \text{ s}^{-1}$ ) and  $\omega$  is the rotation speed of the electrode [47,48].

Koutecky-Levich plot ( $1/j$  vs  $1/\omega^{1/2}$ ) from corresponding LSV can be used to determine  $n$  from the slope (Figures S6 and S7). However,  $n$  values obtained by eq. (3) seems to be more accurate since K-L is an approximation for a multi-step process [49]. According to Figure S7, none of the studied materials shows zero intercept, suggesting the presence of an additional transport limitation, which could explain the absence of a perfect plateau in the diffusion-limited region at high overpotentials (Fig. 3a and Figure S6).

Different kinetic parameters for the ORR obtained from Fig. 3 are summarized in Table 4. Doping with S seems to be a good way for enhancing ORR activity. S-rGO and SN-rGO show  $E_{\text{onset}}$ ,  $E_{1\text{mAcm}^{-2}}^2$  and  $E_{1/2}$  more promising than those of rGO. SN-rGO and Co/SN-rGO develop the best response towards the ORR, since their  $E_{\text{onset}}$  and  $E_{1/2}$  are the ones that most closely approach to the thermodynamic values (1.23 vs. RHE). It should be noted that the error in  $E_{1/2}$  is quite high as the definition of the plateau in the curves is poor, but the trend remains. In addition, better electrochemical performance is observed when doping simultaneously with N and S. Similar sizes of nitrogen and carbon atoms facilitates its insertion in the graphitic structures and the creation of strong N-C bonds. The higher electronegativity of nitrogen atoms and its ability for donating electrons to the  $\pi$  conjugated orbital in graphene structure can polarize the C atom, generating a partial positive charge on it, which makes easier the adsorption of  $\text{O}_2$  molecules, facilitating the ORR [50]. It was also determined the potential at  $1 \text{ mA cm}^{-2}$  for each catalyst. The potential shifts towards more positive values when doping simultaneously with N and S. An improvement on the kinetics can also be observed in the presence of cobalt oxide, reducing the overpotential 50 mV compared to S-rGO and SN-rGO.

Tafel slopes obtained from mass transport corrected Tafel plots (Fig. 3d) are given in Table 4. Different Tafel slopes are obtained at low overpotential region (above 0.8 V) where the ORR is still controlled by the kinetics of the reaction, and at high overpotential (below 0.7 V), where the diffusion starts affecting the ORR. Thus, it is concluded that the ORR mechanism depends on the potential.

A rate determining step (RDS) can be proposed depending on the Tafel slopes. At the low overpotential region, rGO, SN-rGO and Co/SN-rGO exhibit a tafel slope close to 60 mV/decade, indicating that the RDS is a chemical step after an electrochemical one. Considering previous theoretical research, the operating mechanism for the ORR in this type of doped materials is the associative mechanism (see eq. S1-5), where the only chemical step is the first step (eq. S1), which does not agree

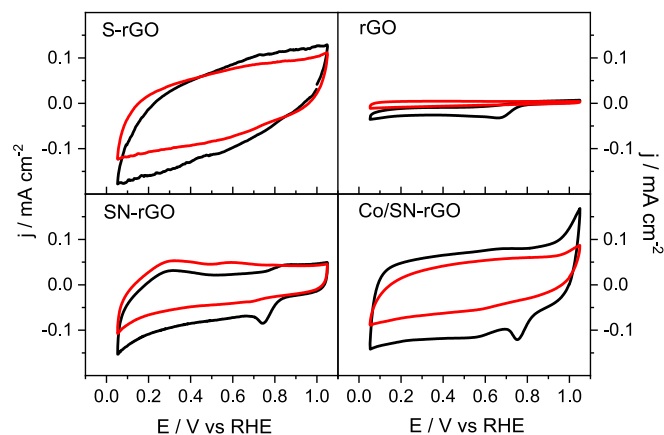
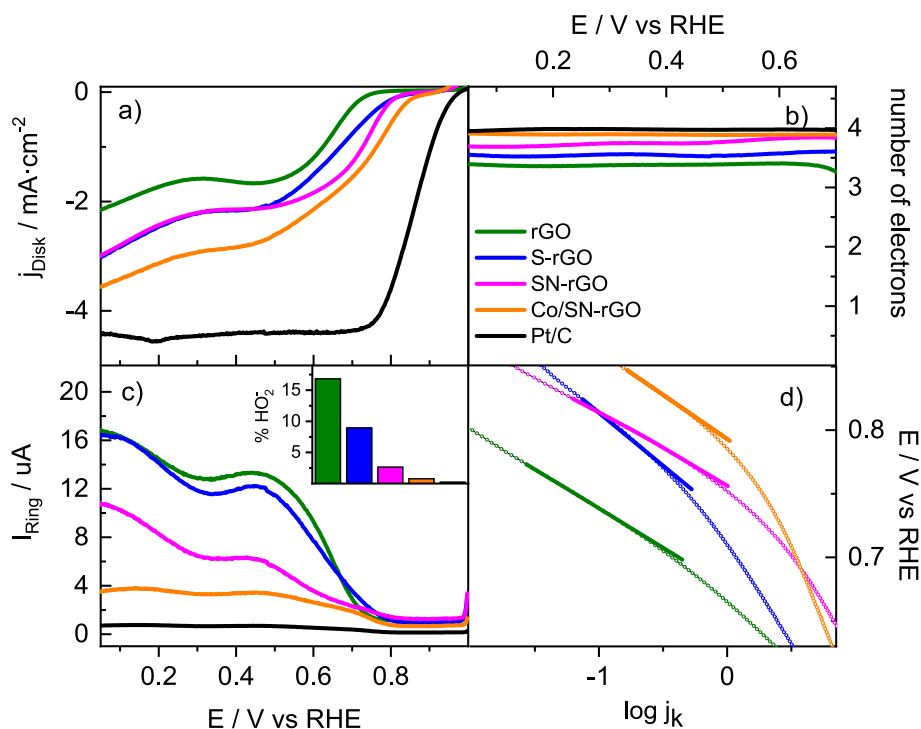


Fig. 2. CVs at  $v = 0.01 \text{ V s}^{-1}$  for all the studied materials in 0.1 M KOH saturated in argon (red) and oxygen (black).



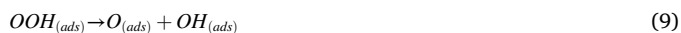
**Fig. 3.** A) LSV at  $v = 0.002 \text{ Vs}^{-1}$  and 1600 rpm in 0.1 M KOH solution for each catalyst; b) number of electrons transferred during the ORR; c) anodic currents recorded at Pt ring at 1.2 V and % of  $\text{HO}_2$  produced at the GMs during the ORR; and d) mass-transport corrected Tafel plots of all materials.

**Table 4**

Electrochemical parameters obtained from LSV and Tafel plots for each catalyst.

Material	$E_{\text{onset}}$ (V)	$E_{1/2}^{\text{mAcM}}$ (V)	$E_{1/2}$ (V)	Tafel slope ( $\text{mV} \cdot \text{dec}^{-1}$ ) low $\eta$
rGO	0.72	0.63	0.64	69
S-rGO	0.81	0.67	0.66	84
SN-rGO	0.81	0.73	0.72	55
Co/SN-rGO	0.86	0.77	0.72	63

with the obtained Tafel slopes [51,52]. Thus, it is necessary to propose a new suitable step for the mechanism. The proposed step is the dissociation of  $\text{OOH}_{(\text{ads})}$  into  $\text{O}_{(\text{ads})} + \text{OH}_{(\text{ads})}$ , replacing eq. S3 for eq. (9)



The higher tafel slope obtained for S-rGO (84 mV/decade) can be explained by the adsorption of  $\text{H}_2\text{O}_2$  specie on the surface of the electrode during the ORR, blocking electroactive sites of the catalyst and giving a tafel slope close to 90 mV/decade [53,54].

At the high overpotential region, slopes between 100 and 250 mV/decade are obtained. A tafel slope of 120 mV/decade indicated the first electro transfer as the RDS, however, the presence of  $\text{H}_2\text{O}_2$  increases can increase the obtained values [53,54].

With the purpose of using the prepared materials at the cathode of a DEFC, the tolerance of the catalysts to the presence of ethanol was studied. Crossover through the membrane, generating a mixed potential at the cathode that generates a loss of fuel cell performance, is a well-known phenomenon in direct alcohol fuel cells, and therefore, low activity towards ethanol is required for the catalysts at this electrode. Thus, a chronoamperometric curve was recorded at 0.60 V after addition of 0.1 M ethanol, at Co/SN-rGO and Pt/C for the sake of comparison (Fig. 4). For Pt/C, a high current is observed in the presence of the alcohol which indicates that a significant loss of catalytic activity towards the ORR would happen with this material; while Co/SN-rGO maintains the current practically unaltered after the injection of the alcohol, and consequently, can be considered as a good candidate for the cathode of a DEFC.

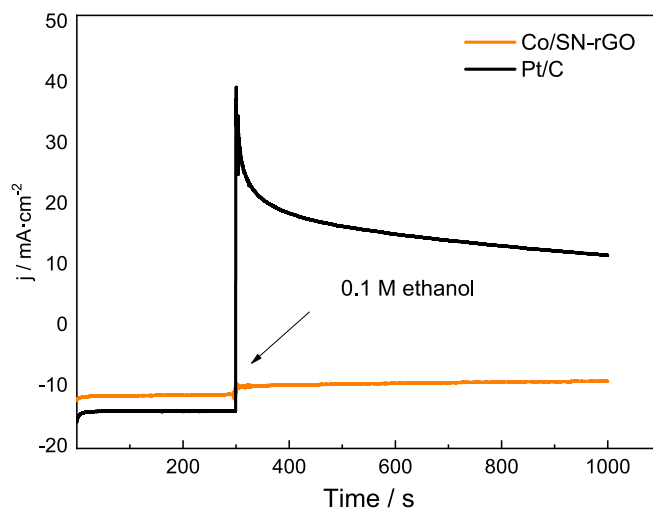


**Fig. 4.** Tolerance test of Co/SN-rGO and Pt/C (20 wt%) towards 0.1 M ethanol solution by chronoamperometric measurement at 0.6 V in oxygen saturated 0.1 M NaOH medium.

### 3.3. DEFC measurements

Electrocatalytic performance of Co/SN-rGO as cathodic material was also evaluated in situ in a DEFC by obtaining the polarization curve in alkaline medium and compared it with a Pt commercial catalyst (Fig. 5). Polarization curves are obtained at  $0.01 \text{ V} \cdot \text{s}^{-1}$  by starting from open circuit potential to 0 V imposing a current through a resistor panel and recording the potential at the same time.

Similar open-circuit potential is observed for both DEFCs, approximately 0.86 V. However, at low overpotentials the first difference appears. At this point, a slightly less pronounced potential drop is observed in the current density, that is, the Co/SN-rGO generates slightly higher current densities with smaller variations of the potential (inset in

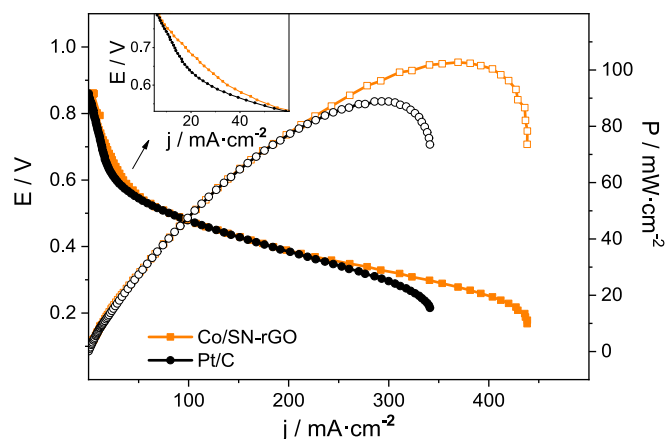


**Fig. 5.** Polarization and power density curves at 90 °C for alkaline DEFC prepared using Co/SN-rGO (orange) and a Pt/C commercial material (black) as cathodic catalyst. Flow rate 2 M ethanol – 2 M KOH = 1 mL/min; flow rate O<sub>2</sub> = 0.2 mL/min.

**Fig. 5).** At intermediate overpotentials (0.8–0.5 V), in the mixed region where activation and ohmic control occurs, lower slope is recorded for the Co/SN-rGO compared to Pt/C, which indicates that the ORR is favored in the catalysts prepared with the graphene substrate. Finally, at high overpotentials (0.4–0.2 V), where the mass transport limitation is dominant and probably the global reaction is diffusion controlled, the Co/SN-rGO presents higher current density values ( $\sim 450 \text{ mA}\cdot\text{cm}^{-2}$ ) than those of platinum catalyst ( $\sim 350 \text{ mA}\cdot\text{cm}^{-2}$ ).

The maximum current density attained in the DEFC is related to the diffusion process of oxygen to the cathode, the amount of catalyst and the electroactive area of the material, but it can also vary depending on its capacity to dislodge the water generated in the cell [2,55]. The hydrophobic properties of graphene materials can be a key point for the removal of water excess that can produce the cathode flooding. The good water management of the Co/SN-rGO cathode that allows a better oxygen diffusion, and the availability of active centers in the material, as well as its large surface area, could be essential factors for the obtained current densities given in Fig. 5.

On the other hand, higher maximum power density ( $100 \text{ mW}\cdot\text{cm}^{-2}$ ) compared to that of Pt ( $80 \text{ mW}\cdot\text{cm}^{-2}$ ) is observed for Co/SN-rGO catalyst. It is interesting to compare the fuel cell performance of this catalyst with other described in the literature [53–59]. Table 5 compares Co/SN-rGO performance with other catalysts reported in the literature [56–62].

**Table 5**

Comparison of catalytic activities of different ORR catalyst in DEFC.

Cathode Catalyst	Anode catalyst	Test conditions	Open circuit voltage (V)	Maximum power density ( $\text{mW}\cdot\text{cm}^{-2}$ )	Reference
Co/SN-rGO	commercial 45 wt% PtRu/C Pt;Ru (2:1) $1 \text{ mg}\cdot\text{cm}^{-2}$	90 °C, 2 M EtOH – 1 M KOH 1 $\text{mL}\cdot\text{min}^{-1}$	0.86	100	This work
(BG-CA-M)-Fe/N/C	20 wt% Pd/C $2.56 \text{ mg}\cdot\text{cm}^{-2}$	90 °C, 2 M EtOH – 1 M KOH at 2 $\text{mL}\cdot\text{min}^{-1}$	0.88	64	[57]
Fe-N-C	PtRu/C 45 wt % $1.33 \text{ mg}\cdot\text{cm}^{-2}$	90 °C, 2 M EtOH – 2 M KOH at 1 $\text{mL}\cdot\text{min}^{-1}$	0.84	62	[58]
Pd <sub>15</sub> (CeO <sub>2</sub> NR) <sub>10</sub> (Vn) <sub>75</sub>	Pd <sub>10</sub> (CeO <sub>2</sub> NR) <sub>20</sub> (Vn) <sub>70</sub> $1 \text{ mg}_{\text{Pd}}\cdot\text{cm}^{-2}$	80 °C, 2 M EtOH – 1 M KOH at 1 $\text{mL}\cdot\text{min}^{-1}$	1.12	65	[59]
Pt/C 40 wt%	PtRu/C 45 wt% $2 \text{ mg}\cdot\text{cm}^{-2}$	90 °C, 1 M EtOH – 1 M KOH at 1 $\text{mL}\cdot\text{min}^{-1}$	1.15	59	[60]
La <sub>0.7</sub> Sr <sub>0.3</sub> MO <sub>3</sub>	PtRu/C Pt;Ru (2:1) $1.5 \text{ mg}\cdot\text{cm}^{-2}$	30 °C, 1 M EtOH – 1 M KOH 10 $\text{mL}\cdot\text{min}^{-1}$	0.873	27.6	[61]
Pd/N&F-C	Pd/N&F-C	60 °C, 2 M EtOH – 1 M KOH 10 $\text{mL}\cdot\text{min}^{-1}$	1.10	570	[62]

It is shown that outstanding performance in alkaline DEFC is observed in the present work for Co/SN-rGO, with higher power density than other proposed catalyst under similar operation conditions.

Short-term durability test was also performed to study the stability of the Co/SN-rGO catalyst layer. Fig. 6 displays the polarization and power density curves recorded at the beginning of the test and after the application of 15 consecutive polarization sequences. The current and power densities obtained at the end of the test present similar values to those obtained for the first curve, which implies a good stability. On the other hand, when the fuel cell operates on fixed current density (25  $\text{mA}\cdot\text{cm}^{-2}$ ) for 6 h, as shown in Fig. 6b, the current and power densities drastically decrease from  $\sim 480 \text{ mA}\cdot\text{cm}^{-2}$  and  $\sim 105 \text{ mW}\cdot\text{cm}^{-2}$  to  $\sim$

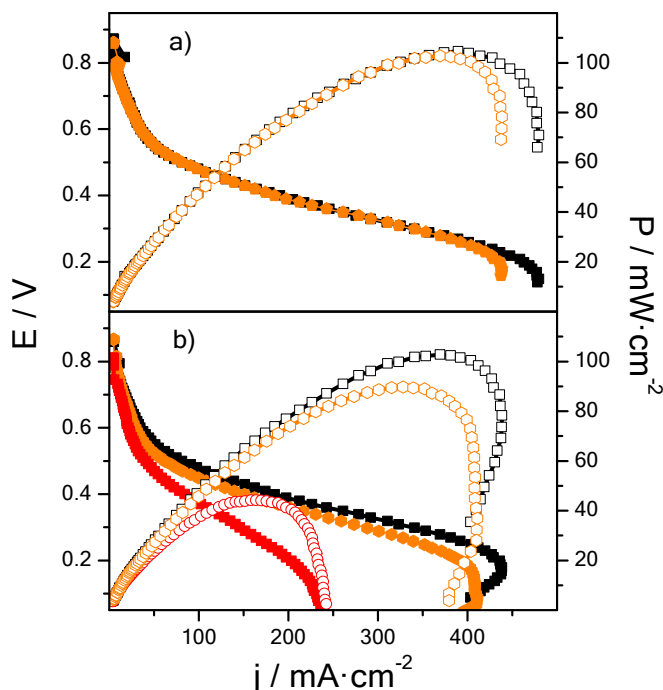


**Fig. 6.** Durability test of DEFC in alkaline medium using Co/SN-rGO as cathode catalyst. a) Polarization and power density curves at the beginning of the test (black) and after 15 consecutive polarization curves (orange); and b) polarization and power density curves at the beginning of the test (black), after operating for 6 h at a constant current density of  $25 \text{ mA}\cdot\text{cm}^{-2}$  (red) and after reactivation (orange).

240 mA·cm<sup>-2</sup> and ~ 44 mW·cm<sup>-2</sup>, respectively. However, after a reactivation procedure consisting in the purge with nitrogen for 15 min, the current and power densities return to ~ 450 mA·cm<sup>-2</sup> and ~ 89 mW·cm<sup>-2</sup> which are close to those obtained at the beginning of the test.

Based on the obtained results, synergistic effect can be observed from the interaction of N and S co-doped, which facilitates the charge transfer process for the ORR. Although the difference in electronegativity between carbon and sulfur is not very large, the atomic size of S is significantly higher than those of N and C. This could be a key factor for generating distortions in the graphene framework which could also contribute to the activity enhancement [26]. Moreover, the polarizability of S atoms provides electron-donor properties to these atoms facilitating the reduction process [27,63]. And lastly, the synergetic effect between N and S atoms reported in the bibliography could explain the excellent electrocatalytic activity of SN-rGO [34,42,63].

Finally, when Co<sub>3</sub>O<sub>4</sub> nanoparticles are supported on SN-rGO surface, an improvement of the ORR kinetic is observed, reducing the production of HO<sub>2</sub><sup>-</sup>, the overpotential, and increasing the cathodic currents during the reduction. Although Co<sub>3</sub>O<sub>4</sub> does not have good ORR electrocatalytic activity by itself, when it is supported on rGO the performance increases due to the conductivity and the electronic properties of the graphene materials [11,37,64].

#### 4. Conclusions

Several reduced graphene oxide materials with different N and S ratios were synthesized by hydrothermal and thermal reduction of graphene oxide. Furthermore, cobalt oxide nanoparticles were anchored to the surface of nitrogen and sulfur co-doped reduced graphene oxide. The electrocatalytic activity of these material for the oxygen reduction reaction varies with the insertion of heteroatoms and nanoparticles into the graphene structure. Tafel slopes analysis indicates a potential dependent mechanism for the ORR in graphene materials. Cyclic and linear sweep voltammetry using a rotating ring-disk electrode show that SN-rGO and Co/SN-rGO are the materials that present better performance for the oxygen electroreduction, being the four electrons pathway the main route during the ORR. Co/SN-rGO displays excellent performance when it is analyzed in a direct ethanol fuel cell test station, pointing lower electron transfer resistance and higher power and current densities than those obtained with a commercial platinum-based catalyst in alkaline media and in the literature for DEFC. Co/SN-rGO also develops a very good stability and durability when studied in a mono-cell, being a good candidate for the cathode of these devices.

#### Declaration of Competing Interest

The authors declare that they have no known competing financial interests or personal relationships that could have appeared to influence the work reported in this paper.

#### Data availability

Data will be made available on request.

#### Acknowledgement

This work has been developed in the framework of the projects PID2020-117586RB-I00, PID2020-112594RB-C33, PID2020-116712RBC21 funded by MCIN/AEI/10.13039/501100011033, and ProID2021010098 funded by the Gobierno de Canarias (FEDER). S. Fajardo acknowledge the MCIN for the pre-doctoral grant (PRE2018-085718). The authors thank SEGAI-ULL for the collaboration.

#### Appendix A. Supplementary data

Supplementary data to this article can be found online at <https://doi.org/10.1016/j.cej.2023.142053>.

#### References

- [1] L. An, T.S. Zhao, Y.S. Li, Carbon-neutral sustainable energy technology: Direct ethanol fuel cells, *Renew. Sustain. Energy Rev.* 50 (2015) 1462–1468, <https://doi.org/10.1016/j.rser.2015.05.074>.
- [2] Y.S. Li, T.S. Zhao, R. Chen, Cathode flooding behaviour in alkaline direct ethanol fuel cells, *J. Power Sources* 196 (2011) 133–139, <https://doi.org/10.1016/j.jpowsour.2010.06.111>.
- [3] J. Wang, Z. Pei, J. Liu, M. Hu, Y. Feng, P. Wang, H. Wang, N. Nie, Y. Wang, C. Zhi, Y. Huang, A high-performance flexible direct ethanol fuel cell with drop-and-play function, *Nano Energy* 65 (2019), 104052, <https://doi.org/10.1016/j.nanoen.2019.104052>.
- [4] L. Osmieri, R. Escudero-Cid, M. Armandi, A.H.A. Monteverde Videla, J.L. García Fierro, P. Ocón, S. Specchia, Fe-N/C catalysts for oxygen reduction reaction supported on different carbonaceous materials. Performance in acidic and alkaline direct alcohol fuel cells, *Appl. Catal. B Environ.* 205 (2017) 637–653.
- [5] T. Varga, G. Ballai, L. Vászrhelyi, H. Haspel, Á. Kukovecz, Z. Kónya, Co<sub>4</sub>N/nitrogen-doped graphene: A non-noble metal oxygen reduction electrocatalyst for alkaline fuel cells, *Appl. Catal. B Environ.* 237 (2018) 826–834, <https://doi.org/10.1016/j.apcatb.2018.06.054>.
- [6] L. An, T.S. Zhao, Transport phenomena in alkaline direct ethanol fuel cells for sustainable energy production, *J. Power Sources* 341 (2017) 199–211, <https://doi.org/10.1016/j.jpowsour.2016.11.117>.
- [7] L.M. Rivera, S. Fajardo, C. Ar, G. Garc, E. Pastor, S- and N-Doped Graphene Nanomaterials for the Oxygen Reduction Reaction, *Catalysts* 7 (2017) 278, <https://doi.org/10.3390/catal7090278>.
- [8] A. Sarapuu, E. Kibena-Pöldsepp, M. Borghei, K. Tammeveski, Electrocatalysis of oxygen reduction on heteroatom-doped nanocarbons and transition metal-nitrogen-carbon catalysts for alkaline membrane fuel cells, *J. Mater. Chem. A* 6 (2018) 776–804, <https://doi.org/10.1039/c7ta08690c>.
- [9] Q. Dehaine, L.T. Tijsseling, H.J. Glass, T. Törmänen, A.R. Butcher, Geometallurgy of cobalt ores: A review, *Miner. Eng.* 160 (2021), <https://doi.org/10.1016/j.mineng.2020.106656>.
- [10] M.M. Hossen, M.S. Hasan, M.R.I. Sardar, J. Bin Haider, Mottakin, K. Tammeveski, P. Atanassov, State-of-the-art and developmental trends in platinum group metal-free cathode catalyst for anion exchange membrane fuel cell (AEMFC), *Appl. Catal. B Environ.* 325 (2022), 121733, <https://doi.org/10.1016/j.apcatb.2023.121733>.
- [11] A. Al Nafey, A. Addad, B. Sieber, G. Chastanet, A. Barras, S. Szunerits, R. Boukherroub, Reduced graphene oxide decorated with Co<sub>3</sub>O<sub>4</sub> nanoparticles (rGO-Co<sub>3</sub>O<sub>4</sub>) nanocomposite: A reusable catalyst for highly efficient reduction of 4-nitrophenol, and Cr(VI) and dye removal from aqueous solutions, *Chem. Eng. J.* 322 (2017) 375–384, <https://doi.org/10.1016/j.cej.2017.04.039>.
- [12] J. Guo, Q. Li, H. Hou, J. Chen, C. Wang, S. Zhang, X. Wang, Cost-effective Co<sub>3</sub>O<sub>4</sub> nanospheres on nitrogen-doped graphene used as highly efficient catalyst for oxygen reduction reaction, *Int. J. Hydrogen Energy* 44 (2019) 30348–30356, <https://doi.org/10.1016/j.ijhydene.2019.09.165>.
- [13] C. Alegro, C. Busacca, A. Di Blasi, O. Di Blasi, A.S. Arico, V. Antonucci, E. Modica, V. Baglio, Electrospun carbon nanofibers loaded with spinel-type cobalt oxide as bifunctional catalysts for enhanced oxygen electrocatalysis, *J. Energy Storage* 23 (2019) 269–277, <https://doi.org/10.1016/j.est.2019.04.001>.
- [14] W. da Silva Freitas, B. Mecheri, C. Lo Vecchio, I. Gatto, V. Baglio, V.C.A. Ficca, A. Patra, E. Placidi, A. D'Epifanio, Metal-organic-framework-derived electrocatalysts for alkaline polymer electrolyte fuel cells, *J. Power Sources* 550 (2022), 232135, <https://doi.org/10.1016/j.jpowsour.2022.232135>.
- [15] D. Wu, T. Wang, L. Wang, D. Jia, Hydrothermal synthesis of nitrogen, sulfur co-doped graphene and its high performance in supercapacitor and oxygen reduction reaction, *Microporous Mesoporous Mater.* 290 (2019), 109556, <https://doi.org/10.1016/j.micromeso.2019.06.018>.
- [16] N. Daems, X. Sheng, I.F.J. Vankelecom, P.P. Pescarmona, Metal-free doped carbon materials as electrocatalysts for the oxygen reduction reaction, *J. Mater. Chem. A* 2 (2014) 4085–4110, <https://doi.org/10.1039/c3ta14043a>.
- [17] L.M. Rivera, G. García, E. Pastor, Novel graphene materials for the oxygen reduction reaction, *Curr. Opin. Electrochem.* 9 (2018) 233–239, <https://doi.org/10.1016/j.coelec.2018.05.009>.
- [18] D. Sebastián, A. Serov, I. Matanovic, K. Artyushkova, P. Atanassov, A.S. Arico, V. Baglio, Insights on the extraordinary tolerance to alcohols of Fe-N-C cathode catalysts in highly performing direct alcohol fuel cells, *Nano Energy* 34 (2017) 195–204, <https://doi.org/10.1016/j.nanoen.2017.02.039>.
- [19] M. Chen, L. Wang, H. Yang, S. Zhao, H. Xu, G. Wu, Nanocarbon/oxide composite catalysts for bifunctional oxygen reduction and evolution in reversible alkaline fuel cells: A mini review, *J. Power Sources* 375 (2018) 277–290, <https://doi.org/10.1016/j.jpowsour.2017.08.062>.
- [20] L. Dai, Y. Xue, L. Qu, H.J. Choi, J.B. Baek, Metal-Free Catalysts for Oxygen Reduction Reaction, *Chem. Rev.* 115 (2015) 4823–4892, <https://doi.org/10.1021/cr5003563>.
- [21] I.C. Man, I. Trancă, S.G. Soriga, First principle studies of oxygen reduction reaction on N doped graphene: Impact of N concentration, position and co-adsorbate effect, *Appl. Surf. Sci.* 510 (2020), <https://doi.org/10.1016/j.apsusc.2020.145470>.
- [22] C. Maouche, Y. Zhou, B. Li, C. Cheng, Y. Wu, J. Li, S. Gao, J. Yang, Thermal treated three-dimensional N-doped graphene as efficient metal free-catalyst for oxygen reduction reaction, *J. Electroanal. Chem.* 853 (2019), 113536, <https://doi.org/10.1016/j.jelechem.2019.113536>.



- [23] L. Zhang, J. Niu, L. Dai, Z. Xia, Effect of microstructure of nitrogen-doped graphene on oxygen reduction activity in fuel cells, *Langmuir*. 28 (2012) 7542–7550, <https://doi.org/10.1021/la2043262>.
- [24] L. Zhang, Z. Xia, Mechanisms of oxygen reduction reaction on nitrogen-doped graphene for fuel cells, *J. Phys. Chem. C*. 115 (2011) 11170–11176, <https://doi.org/10.1021/jp201991j>.
- [25] R. Sibul, E. Kibena-Pöldsepp, U. Mäeorg, M. Merisalu, A. Kikas, V. Kisand, A. Treshchalov, V. Sammelselg, K. Tammeveski, Sulphur and nitrogen co-doped graphene-based electrocatalysts for oxygen reduction reaction in alkaline medium, *Electrochem. Commun.* 109 (2019), 106603, <https://doi.org/10.1016/j.elecom.2019.106603>.
- [26] M. Klingele, C. Pham, K.R. Vuyyuru, B. Britton, S. Holdcroft, A. Fischer, S. Thiele, Sulfur doped reduced graphene oxide as metal-free catalyst for the oxygen reduction reaction in anion and proton exchange fuel cells, *Electrochem. Commun.* 77 (2017) 71–75, <https://doi.org/10.1016/j.elecom.2017.02.015>.
- [27] Z. Wang, P. Li, Y. Chen, J. He, W. Zhang, O.G. Schmidt, Y. Li, Pure thiophene-sulfur doped reduced graphene oxide: Synthesis, structure, and electrical properties, *Nanoscale*. 6 (2014) 7281–7287, <https://doi.org/10.1039/c3nr05061k>.
- [28] Y. Zhao, C. Zhang, T. Liu, R. Fan, Y. Sun, H. Tao, J. Xue, Low temperature green synthesis of sulfur-nitrogen co-doped graphene as efficient metal-free catalysts for oxygen reduction reaction, *Int. J. Electrochem. Sci.* 12 (2017) 3537–3548, <https://doi.org/10.20964/2017.04.67>.
- [29] Y. Chen, Z. Shi, S. Li, J. Feng, B. Pang, L. Yu, W. Zhang, L. Dong, N. S-codoped graphene supports for Ag-MnFe<sub>2</sub>O<sub>4</sub> nanoparticles with improved performance for oxygen reduction and oxygen evolution reactions, *J. Electroanal. Chem.* 860 (2020), 113930, <https://doi.org/10.1016/j.jelechem.2020.113930>.
- [30] N. Iwashita, C.R. Park, H. Fujimoto, M. Shiraiishi, M. Inagaki, Specification for a standard procedure of X-ray diffraction measurements on carbon materials, *Carbon* N. Y. 42 (2004) 2131, <https://doi.org/10.1016/j.carbon.2004.05.027>.
- [31] P. Wang, M. Gao, H. Pan, J. Zhang, C. Liang, J. Wang, P. Zhou, Y. Liu, A facile synthesis of Fe<sub>3</sub>O<sub>4</sub>/C composite with high cycle stability as anode material for lithium-ion batteries, *J. Power Sources*. 239 (2013) 466–474, <https://doi.org/10.1016/j.jpowsour.2013.03.073>.
- [32] P. Tan, B. Chen, H. Xu, W. Cai, W. He, M. Ni, In-situ growth of Co<sub>3</sub>O<sub>4</sub> nanowire-assembled clusters on nickel foam for aqueous rechargeable Zn-Co<sub>3</sub>O<sub>4</sub> and Zn-air batteries, *Appl. Catal. B Environ.* 241 (2019) 104–112, <https://doi.org/10.1016/j.apcatb.2018.09.017>.
- [33] C. Botas, P. Álvarez, C. Blanco, R. Santamaría, M. Granda, P. Ares, F. Rodríguez-Reinos, R. Menéndez, The effect of the parent graphite on the structure of graphene oxide, *Carbon* N. Y. 50 (2012) 275–282, <https://doi.org/10.1016/j.carbon.2011.08.045>.
- [34] S. Bag, B. Mondal, A.K. Das, C.R. Raj, Nitrogen and sulfur dual-doped reduced graphene oxide: Synergistic effect of dopants towards oxygen reduction reaction, *Electrochim. Acta*. 163 (2015) 16–23, <https://doi.org/10.1016/j.electacta.2015.02.130>.
- [35] D.M. Fernandes, P. Mathumba, A.J.S. Fernandes, E.I. Iwuoha, C. Freire, Towards efficient oxygen reduction reaction electrocatalysts through graphene doping, *Electrochim. Acta*. 319 (2019) 72–81, <https://doi.org/10.1016/j.electacta.2019.06.175>.
- [36] E.F. Sheka, Y.A. Golubev, N.A. Popova, Graphene domain signature of raman spectra of sp<sup>2</sup> amorphous carbons, *Nanomaterials*. 10 (2020) 1–22, <https://doi.org/10.3390/nano10102021>.
- [37] T. Zhang, C. He, F. Sun, Y. Ding, M. Wang, L. Peng, J. Wang, Y. Lin, Co<sub>3</sub>O<sub>4</sub> nanoparticles anchored on nitrogen-doped reduced graphene oxide as a multifunctional catalyst for H<sub>2</sub>O<sub>2</sub> reduction, oxygen reduction and evolution reaction, *Sci. Rep.* 7 (2017) 43638, <https://doi.org/10.1038/srep43638>.
- [38] D.W. Wang, D. Su, Heterogeneous nanocarbon materials for oxygen reduction reaction, *Energy Environ. Sci.* 7 (2014) 576–591, <https://doi.org/10.1039/c3ee43463j>.
- [39] M.A. Molina-García, N.V. Rees, “Metal-free” electrocatalysis: Quaternary-doped graphene and the alkaline oxygen reduction reaction, *Appl. Catal. A Gen.* 553 (2018) 107–116, <https://doi.org/10.1016/j.apcata.2017.12.014>.
- [40] P. Zhang, J.S. Wei, X.B. Chen, H.M. Xiong, Heteroatom-doped carbon dots based catalysts for oxygen reduction reactions, *J. Colloid Interface Sci.* 537 (2019) 716–724, <https://doi.org/10.1016/j.jcis.2018.11.024>.
- [41] B. Murugesan, N. Pandiyan, M. Arumugam, M. Veerasingam, J. Sonamuthu, A. R. Jeyaraman, S. Samayanan, S. Mahalingam, Two dimensional graphene oxides converted to three dimensional P, N, F and B, N, F tri-doped graphene by ionic liquid for efficient catalytic performance, *Carbon* N. Y. 151 (2019) 53–67, <https://doi.org/10.1016/j.carbon.2019.05.060>.
- [42] M. Sahoo, S. Ramaprabhu, Nitrogen and sulfur co-doped porous carbon – is an efficient electrocatalyst as platinum or a hoax for oxygen reduction reaction in acidic environment PEM fuel cell? *Energy*. 119 (2017) 1075–1083, <https://doi.org/10.1016/j.energy.2016.11.066>.
- [43] L.S. Sundar, G.O. Iruetueta, E. Venkata Ramana, M.K. Singh, A.C.M. Sousa, Case Studies in Thermal Engineering Thermal conductivity and viscosity of hybrid nanofluids prepared with magnetic nanodiamond-cobalt oxide (ND-Co 3 O 4) nanocomposite, *Case Stud. Therm. Eng.* 7 (2016) 66–77.
- [44] L. Xu, Q. Jiang, Z. Xiao, X. Li, J. Huo, S. Wang, L. Dai, Plasma-Engraved Co<sub>3</sub>O<sub>4</sub>Nanosheets with Oxygen Vacancies and High Surface Area for the Oxygen Evolution Reaction, *Angew. Chemie - Int. Ed.* 55 (2016) 5277–5281, <https://doi.org/10.1002/anie.201600687>.
- [45] R. Zhang, M. Tahir, S. Ding, M.A. Qadeer, H. Li, Q.X. Zeng, R. Gao, L. Wang, X. Zhang, L. Pan, J.J. Zou, Promotion of Nitrogen Reserve and Electronic Regulation in Bamboo-like Carbon Tubules by Cobalt Nanoparticles for Highly Efficient ORR, *ACS Appl. Energy Mater.* 3 (2020) 2323–2330, <https://doi.org/10.1021/acsaeem.9b01617>.
- [46] Y. Xiao, J. Hong, X. Wang, T. Chen, T. Hyeon, W. Xu, Revealing Kinetics of Two-Electron Oxygen Reduction Reaction at Single-Molecule Level, *J. Am. Chem. Soc.* 142 (2020) 13201–13209, <https://doi.org/10.1021/jacs.0c06020>.
- [47] N.R. Elezović, B.M. Babić, L.J.M. Vračar, N.V. Krstajić, Oxygen reduction at platinum nanoparticles supported on carbon cryogel in alkaline solution, *J. Serbian Chem. Soc.* 72 (2007) 699–708, <https://doi.org/10.2298/JSC0707699E>.
- [48] S. Treimer, A. Tang, D.C. Johnson, A consideration of the application of Koutecký-Levich plots in the diagnoses of charge-transfer mechanisms at rotated disk electrodes, *Electroanalysis*. 14 (2002) 165–171, [https://doi.org/10.1002/1521-4109\(200202\)14:3<165::AID-ELAN165>3.0.CO;2-6](https://doi.org/10.1002/1521-4109(200202)14:3<165::AID-ELAN165>3.0.CO;2-6).
- [49] R. Zhou, Y. Zheng, M. Jaroniec, S.Z. Qiao, Determination of the Electron Transfer Number for the Oxygen Reduction Reaction: From Theory to Experiment, *ACS Catal.* 6 (2016) 4720–4728, <https://doi.org/10.1021/acscatal.6b01581>.
- [50] Q. Lv, W. Si, J. He, L. Sun, C. Zhang, N. Wang, Z. Yang, X. Li, X. Wang, W. Deng, Y. Long, C. Huang, Y. Li, Selectively nitrogen-doped carbon materials as superior metal-free catalysts for oxygen reduction, *Nat. Commun.* 9 (2018), <https://doi.org/10.1038/s41467-018-05878-y>.
- [51] L. Yu, X. Pan, X. Cao, P. Hu, X. Bao, Oxygen reduction reaction mechanism on nitrogen-doped graphene: A density functional theory study, *J. Catal.* 282 (2011) 183–190, <https://doi.org/10.1016/j.jcat.2011.06.015>.
- [52] M.H. Shao, P. Liu, R.R. Adzic, Superoxide anion is the intermediate in the oxygen reduction reaction on platinum electrodes, *J. Am. Chem. Soc.* 128 (2006) 7408–7409, <https://doi.org/10.1021/ja061246s>.
- [53] C.F. Zinola, A.M. Castro Luna, W.E. Triaca, A.J. Arvia, Electroreduction of molecular oxygen on preferentially oriented platinum electrodes in acid solution, *J. Appl. Electrochem.* 24 (1994) 119–125, <https://doi.org/10.1007/BF00247782>.
- [54] G. Pérez, E. Pastor, C.F. Zinola, A novel Pt/Cr/Ru/C cathode catalyst for direct methanol fuel cells (DMFC) with simultaneous methanol tolerance and oxygen promotion, *Int. J. Hydrogen Energy*. 34 (2009) 9523–9530, <https://doi.org/10.1016/j.ijhydene.2009.09.088>.
- [55] D. Saebaa, C. Chaiburi, S. Authayanun, Model based evaluation of alkaline anion exchange membrane fuel cells with water management, *Chem. Eng. J.* 374 (2019) 721–729, <https://doi.org/10.1016/j.cej.2019.05.200>.
- [56] L. Osmieri, L. Pezzolato, S. Specchia, Recent trends on the application of PGM-free catalysts at the cathode of anion exchange membrane fuel cells, *Curr. Opin. Electrochem.* 9 (2018) 240–256, <https://doi.org/10.1016/j.coelec.2018.05.011>.
- [57] M. Rauf, R. Chen, Q. Wang, Y.C. Wang, Z.Y. Zhou, Nitrogen-doped carbon nanotubes with encapsulated Fe nanoparticles as efficient oxygen reduction catalyst for alkaline membrane direct ethanol fuel cells, *Carbon* N. Y. 125 (2017) 605–613, <https://doi.org/10.1016/j.carbon.2017.09.093>.
- [58] L. Osmieri, R. Escudero-Cid, A.H.A. Monteverde Videla, P. Ocón, S. Specchia, Application of a non-noble Fe-N-C catalyst for oxygen reduction reaction in an alkaline direct ethanol fuel cell, *Renew. Energy*. 115 (2018) 226–237, <https://doi.org/10.1016/j.renene.2017.08.062>.
- [59] V.S. Pinheiro, F.M. Souza, T.C. Gentil, L.S. Parreira, B.L. Batista, M.C. Santos, Hybrid palladium-ceria nanorod electrocatalysts applications in oxygen reduction and ethanol oxidation reactions in alkaline media, *Int. J. Hydrogen Energy*. 46 (2021) 15896–15911, <https://doi.org/10.1016/j.ijhydene.2021.02.056>.
- [60] H. Hou, S. Wang, W. Jin, Q. Jiang, L. Sun, L. Jiang, G. Sun, KOH modified Nafion112 membrane for high performance alkaline direct ethanol fuel cell, *Int. J. Hydrogen Energy*. 36 (2011) 5104–5109, <https://doi.org/10.1016/j.ijhydene.2010.12.093>.
- [61] I. Grimmer, P. Zorn, S. Weinberger, C. Grimmer, B. Pichler, B. Cermenek, F. Gebetsroither, A. Schenk, F.A. Mautner, B. Bitschnau, V. Hacker, Ethanol tolerant precious metal free cathode catalyst for alkaline direct ethanol fuel cells, *Electrochim. Acta*. 228 (2017) 325–331, <https://doi.org/10.1016/j.electacta.2017.01.087>.
- [62] J. Chang, G. Wang, M. Wang, Q. Wang, B. Li, H. Zhou, Y. Zhu, W. Zhang, M. Omer, N. Orlovskaya, Q. Ma, M. Gu, Z. Feng, G. Wang, Y. Yang, Improving Pd–N–C fuel cell electrocatalysts through fluorination-driven rearrangements of local coordination environment, *Nat. Energy*. 6 (2021) 1144–1153, <https://doi.org/10.1038/s41560-021-00940-4>.
- [63] J. Xu, G. Dong, C. Jin, M. Huang, L. Guan, Sulfur and nitrogen co-doped, few-layered graphene oxide as a highly efficient electrocatalyst for the oxygen-reduction reaction, *ChemSusChem*. 6 (2013) 493–499, <https://doi.org/10.1002/cssc.201200564>.
- [64] H.P. Uskaikar, N.P. Shetti, S.J. Malode, Electrocatalytic reduction of oxygen on Co<sub>3</sub>O<sub>4</sub>: Effects of processing method, *Mater. Sci. Energy Technol.* 1 (2018) 129–135, <https://doi.org/10.1016/j.mset.2018.06.006>.